Failure Analysis of Superheater Tube

A. Movahedi-Rad[a], S.S. Plasseyed[b,c], M. Attarian[b,c]*

a: School of Metallurgical and Materials Engineering, College of Engineering,
University of Tehran, Tehran, Iran
b: Razi Metallurgical Research Center (RMRC), Tehran, Iran
c: Department of Materials Science and Engineering, Sharif University of Technology, Tehran, Iran

*Corresponding author: e-mail: m_attarian@razi-center.net
Phone: +98 214683157077, Fax: +98 2146831597

Abstract

The failure analysis of a ruptured superheater tube after 20 years service in the oil-fueled boiler, as the typical problems in power plants, was investigated. A thin-lipped rupture at failed region was observed in superheater tube. By measuring the tube's wall thicknesses far from failed region, non-uniformity was seen. The suggested main root cause of failure was fireside corrosion of the tube during the service. Because of low grade of used fuel, sodium, sulfur, and vanadium elements were observed at the outer surface, which caused continuously scale formation and reduction of wall thickness, by metal consumption. In addition, it seems that it has been worsened by occurrence of long-term overheating. Coagulation of carbides at both outer and inner regions of tube was observed that could prove the occurrence of overheating during the service. In addition, the formation of sigma-phase particles was revealed because of being in the susceptible temperature after 20 years in service. At the end, in order to prevent or decelerate such failure, some recommended remedies were suggested.

1. Introduction

Energy is one of the most important issues all over the world. Among many energy sources, power plants and heat-exchangers are very essential. Superheaters are one of the most critical components in heat-exchanger application [1]. The main advantage of using superheater tubes is reducing fuel consumption. However, the superheater tubes are vulnerable to the particular types of failure such as creep failure, distortion, and mechanical- environmental induced failure [2]. It has been reported that the superheaters have the highest failure location all cross the world [3]. So, it is extremely important to determine and correct the possible causes of failures.

There are several investigations in the literature, which have reported failure in superheater tubes. Chandra *et al.* [4] studied the fireside corrosion of 2.25Cr-1Mo carbon steel superheater tubes that used in a circulating fluidized bed combustion boiler. In another work, the effect of surface defects produced by water vapour oxidation in steels was investigated [5]. They characterized the surface defects that commonly used in fossil power plants. Jones [3] also reported the failure of four internally pressurized tubes involving a superheater that had been failed by creep. Another research by Psyllaki *et al.* [6] on the metallurgical evaluation of creep-failed superheater tubes showed the metallurgical modifications during high-temperature exposure of a steel pipeline led to a local material's failure. Some researchers also identified the failure of superheater tubes by performing finite element (FEM) method [7,8]. In another investigation, failure analysis of failed superheater tube was presented by using an empirical formula beside visual inspections and metallurgical examinations [9]. It must be considered that a failure of tube is generally a sign of another problems and it needs complete evaluations and investigations.

In this study, in the power plant with oil-fueled boiler, a failure analysis of seamless superheater tube is comprehensively investigated, feasible influential factors have been considered, and some remedies are recommended. The tube material was austenitic stainless steel with intended operating temperature of 538 °C, which was applied continuously. The average steam pressure was reported equal to 18 MPa and the nominal wall thickness of superheater tube was 5.7 mm.

2. Experimental procedure

In order to find out the failure mechanism, at first, the actual chemical composition was determined by using spectroscopy method. Then, wall thickness measurements were done for assessing the impact of operational situation on the tube's wall thickness. Two samples were cut far from the failed region (Sample A) and other sample at the failed region (Sample B). The samples were polished and etched with Glycergia solution for studying tube's microstructure by optical microscopy and scanning electron microscope (SEM). In addition, another longitudinal section was cut and prepared by using electro-etch method in order to understand the presence of sigma-phase. Microanalysis was carried out by Energy dispersive X-ray spectroscopy (EDS). In addition, microhardness measurements at the outer and inner sides of tube in transverse section and at mid-walls in longitudinal section away from the rupture section were carried out.

3. Results and discussion

3.1. Visual inspections

The ruptured tube shows bulging and plastic deformation at the failure site which are exhibited in Fig. 1 (a). In Fig. 1 (b), a white scale on external surface of the tube is observable. Fig. 2 shows wall thickness measurements for three sections of tubes, first transverse cross-section and longitudinal section far from failed region are shown by arrow A in Fig. 1 (a). It is seen that the tube's thickness has been reduced non-uniformly and wall thinning has been happened as can be seen in Fig. 2 (a). Also, by observing the wall thickness of longitudinal section in Fig. 2 (b), it can be understood that the non-uniformity in wall thickness has taken place from the one side (fireside) of the tube. Secondly, in Fig. 2 (c), the thickness of tube at the failed region is shown. In the failed region, a thin-lipped rupture was formed because of the swelling of the tube and significantly decreasing of the wall thickness.

3.2. Chemical composition and microscopic examinations

Portion of tube was tested for chemical analysis by using spectroscopy method. Table 1 summarizes the chemical composition of superheater tube that meets the requirements of

American standard ASTM A213 Grade-TP347H. It covers seamless austenitic stainless steel boiler, superheater, and heat-exchanger tubes.

To microstructural examination, two specimens were cut away from the failed region (Sample A) and near the failed region (Sample B). Specimens were etched and microstructural observations at the mid-wall location are shown in Fig. 3 in two magnifications. The microstructure consists of austenitic grains with twining and fine distributed $M_{23}C_6$ carbides precipitation at the grain boundaries and matrix. The presence of these phases is typical for austenitic stainless steels. However, further observation reveals the existence of new particles, which are located at the grain boundaries. The transverse cross-section SEM image at mid-wall location and corresponding EDS analysis results are shown in Fig. 4 and Fig. 5, respectively. Accordingly, the scattered niobium carbide (arrow A) and chromium rich particles, which are located at grain boundaries (arrow B) are detected. In order to observe and identify the existence of sigma-phase particles in the microstructure, a longitudinal section was cut and prepared by using electro-etch method. In Fig. 6 and Fig. 7, a SEM micrograph and corresponding EDS results are shown, respectively. As can be seen, the sigma-phase particles have been precipitated after long period of service. The existence of the sigma-phase particles can be certified by considering similar observations in literature [10]. Also, based on the EDS results, the chemical composition of these particles is close to FeCr, as a typical chemical composition of sigma-phase particles. It has been reported that the amount of sigma-phase is a function of operating time and temperature and chemical composition of material [11]. The temperature range where sigma-phase forms varies with chemical composition of metals, but in general, it can be stated that it forms at temperatures from 565 °C to 980 °C [12].

The SEM micrographs of outer and inner diameter sides of tube are shown in Fig. 8. As can be seen, a scale has been formed during the long-term service. In Fig. 8 (a), it is displayed that the external superficial scale consists of two layers. Based on the EDS analysis results, which are displayed in Fig. 9, both layers are a combination of chromic and ferrous oxidations, however, the concentration of oxygen is higher in the layer (I) and

4

vanadium is also characterized. In order to better identification of oxides on the outer surface, the loose sheets of scales were cut and related EDS result is shown in Fig. 10. As can be seen, the substantial amount of sodium, sulfur, and vanadium has been gathered during the operation. The traces of the ash deposit are a physical consequence of the use of the fuel. In other words, the presence of these elements is related to poor and incomplete fuel combustion conditions, which has initiated hot corrosion. In this studied, Mazut has been used as a fuel for firing and Table 2 summarizes the details of its chemical composition. The main difference between the different types of Mazut is the content of sulfur. Accordingly, the used fuel is classified as a high sulfur mazut. In addition, the considerable amounts of Na and V elements present in the fuel. Here, it is worth noting to state the effect of low grade of fuel on firing. In combustion products of fuel oil, sulfur is typically present as Na_2SO_4. At high temperature, in a typical hot corrosion reaction, molten Na_2SO_4 induced corrosion attack involves salt fluxing and sulfidation [13]. Another problematic impurity is vanadium which causes some corrosion problems due to the formation of V_2O_5 with a melting point of 690 °C [14,15]. The situation is worsened when V-Na mixed oxides with low meting point of 550 °C are formed during the service and make the tube vulnerable for more rapid hot corrosion [15]. These compounds with low melting point create a molten flux at service temperature (T < 600 °C) which attacks and removes the protective oxide scale, exposing more base metals. As a result, continuous metal consumption and wall-thinning have led the tube to non-uniform wall thickness and finally to the failure. In order to support the likelihood of fireside corrosion mechanism, the ratio of average wall loss to steamside scale thickness was measured 29.5. This value is much higher than 5 which confirms the activation of fireside corrosion mechanism.

With regard to overheating, there are some possible factors such as steamside scale, condition of the site, and excessive temperature at operating condition. The accumulation of scales with a lower thermal conductivity in comparison to the steel tube metal increases the metal temperature and this can accelerate further corrosion and oxidation. In this study, the steamside scale size of tube is maximally 150 μm at the failed region.

5

There are a number of published algorithms available for estimating metal temperature from oxide thickness data. According to the Dr. French's time-temperature-oxide relationship [16], steamside scale seems to be relatively thin and normal and is not thick enough to cause overheating. However, it certainly contributes to the temperature increase in some degrees.

The coagulation and growth of carbides happened at both outer and inner sides of tube, which located continuously at the grain boundaries. The formation of these grain boundary carbides can somehow show the existence of high operating temperature and occurrence of overheating during the operation. In other words, the diffusion of carbon in stainless steel results in the carbides formation at high temperature. Although there was not any temperature monitoring in the power plant during the service, the growth of chromium carbides at gain boundaries can indicate the tube has been held at high temperatures due to the insolubility of chromium at these temperatures. In addition, it has been reported that the degree of carburization is governed by the levels of carbon and oxygen in the gas, the temperature and the steel composition [17]. In order to have an extensive observation, two optical micrographs are attached and shown in Fig. 11. Recent figure evidently illustrates the incremental trend of carbides coagulation near the both surfaces. Also, as can be seen, these carbides are restricted to the grain boundaries. Therefore, it is suggested that long-term overheating has aggravated the failure of tube.

The SEM observation was also prepared from the failed region (Sample B) and shown in Fig. 12. It is seen that some microcracks present at the tip of failed region. Furthermore, some voids are appeared at the fracture lip and a very thick scale (150 μm) at the inner surface of the failed region demonstrates a severe degradation of the tube material during 20 years of operation in fireside region of tube.

3.3. Microhardness results

The variation of micro hardness against distance at outer and inner surfaces is depicted in Fig. 13 at locations away from the failed region. The micro-hardness test was done with respect to the ASTM E10-12 standard. As can be seen, the values of hardness decrease

after a little distance from the both surfaces and reach to a steady state at mid-wall locations; nonetheless, it decreases steeply by retreating from the outer surface. These higher values of hardness are well correlated with changes in the volume fraction of coagulated carbides at outer and inner surfaces, which were shown in Fig. 11. In the other words, these downward trends of hardness values are an evidence of carburization in tube at the both inner and outer sides. The hardness measurements have been taken at mid-walls away from the rupture section at the thin side of tube. The results of hardness at 9 points are shown in Fig. 14. It is evident that the hardness values are nearly equal at the mid-wall of the tube, which shows the activation of fireside corrosion mechanism.

3.4. Recommended remedies

Some suggested remedies are also recommended so that to prevent or decelerate this type of failure. The first solution for preventing such failure is fuel selection. Using higher qualified fuels with lower quantities of vanadium, sulfur, and sodium will be the most important suggested remedy. Most natural and manufactured gaseous fuels are ashless, whereas most oils have ash contents. However, using of high sulfur and vanadium fuels sometimes cannot be avoided. Therefore, continuous and closed control on operating conditions is mandatory. In addition, periodic ash removal should also be considered as practical way for increasing tubes' life. Ash removal prevents development of material degradation conditions. Using fuel additives such as powdered magnesia, dolomite, and alumina is a complementary preventing method, which promotes the formation of ash deposits that are easily removed.

4. Conclusions

The failure analysis of ASTM A213 Grade-TP347H superheater tube in an oil-fueled boiler power plant was investigated in order to determine the failure mechanism and failure root cause by doing visual observations, thickness measurements, microstructural studies, and microhardness test. In this study, the main root of failure was fireside corrosion of the tube during the service because of low grade of used fuel. The thin-lipped rupture at failed region and non-uniform wall thickness far from fail region were observed. The ratio of average wall loss to steamside scale thickness was considerably

higher than 5 which supported the likelihood of fireside corrosion. The coagulation of carbides at both outer and inner regions showed the high service temperature. So, in this study, it was suggested that the fireside corrosion was the main root cause of the failure which had been worsened by occurrence of long-term overheating.

References

[1] French David N. Metallurgical failures in fossil fired boilers. New York: A Wiley-Interscience Publication, John Wiley & Sons Inc.; 2000.

[2] ASM metals handbook. Failure analysis and prevention, vol. 11. Materials Park (OH): ASM International; 1992.

[3] Jones DRH. Creep failures of overheated boiler, superheater and reformer tubes. Eng Fail Anal 2004;11:873–93.

[4] Chandra K, Kain V, Dey GK. Failure of 2.25Cr–1Mo steel superheater tubes in a fluidized bed combustor due to fireside corrosion. Mater Charact 2011;62:62–9.

[5] Rodrıguez R, Martın-Meizoso A, Ocana I, Martınez-Esnaola JM, Perez AS, Izquierdo J. Standard surface defects produced by water vapour oxidation in steels used in fossil fuel fired power plants. Mat Sci Eng A 2003;342:1-10.

[6] Psyllaki PP, Pantazopoulos G, Lefakis H. Metallurgical evaluation of creep-failed superheater tubes. Eng Fail Anal 2009;16:1420–31.

[7] Othman H, Purbolaksono J, Ahmad B. Failure investigation on deformed superheater tubes. Eng Fail Anal 2009;16:329–39.

[8] Purbolaksono J, Ahmad J, Beng LC, Rashid AZ, Khinani K, Ali AA. Failure analysis on a primary superheater tube of a power plant. Eng Fail Anal 2010;17:158–67.

[9] Rahman MM, Purbolaksono J, Ahmad J. Root cause failure analysis of a division wall superheater tube of a coal-fired power station. Eng Fail Anal 2010;17:1490–4.

[10] Plaut RL, Herrera C, Escriba DM. Mater. Res. 2007;10: 453-460.

[11] Senior BA. Effect of phase transformation on the creep rupture properties of two type 316 weld metals. J Mater Sci 1990;25:45-53.

[12] Vander Voort GF. Embrittlement of steels in metals handbook volume 1. 1st ed. ASM International;1990.

[13] Brnstein, N.S, DesGrescenti, M.A., (1971), Met. Trans., **2**, 2875.

[14] Swisher, J.H. and Shankarnarayan, S., (1994), Inhibiting Vanadium Induced Corrosion, Materials Performance, **33** (9), 49.

[15] Young D. High temperature oxidation and corrosion of metals. 1st ed. Elsevier; 2008.

[16] French D.N., Metallurgical Failures in Fossil Fired Boilers, John Wiley & Sons, New York, 1983.

[17] Simonetti S, Lanz C, Brizuela G, Juan A. Study of the 1.25Cr–1Mo–0.25V steel microstructure after a carburization phenomenon. Eng Fail Anal 2010;527:5755–60.

Figures and tables' captions:

Table 1. Chemical composition of tube
Table 2. The details of oil composition used for firing
Fig. 1. (a) Ruptured region of as-received superheater tube, and (b) the presence of white deposits on external surface.
Fig. 2. Thickness measurements for two sections of tube, (a) transverse cross-section far from failed region, and (b) failed region.
Fig. 3. Optical micrographs at mid-wall location of superheater tube far from failed region.
Fig. 4. SEM micrographs of transverse cross-section at mid-wall location.
Fig. 5. Corresponding EDS results of (a) arrow (A), and (b) arrow (B) in Fig. 4.
Fig. 6. SEM micrographs of longitudinal section.
Fig. 7. Corresponding EDS results of sigma-phase particles in Fig. 6.
Fig. 8. SEM micrographs at the (a) outer diameter side, and (b) inner diameter side of tube.
Fig. 9. Corresponding EDS results of (a) layer (I), and layer (II) in Fig. 8 (a).
Fig. 10. EDS analysis of loose scales on the external surface of tube.
Fig. 11. Optical micrographs of (a) outer diameter, and (b) inner diameter of tube in order to illustrate incremental coagulation of carbides with approaching to the tube's surfaces.
Fig. 12. SEM micrographs of failed region.
Fig. 13. Variation of microhardness against distance from (a) outer surface, and (b) inner surface.
Fig. 14. The hardness measurements at some mid-walls away from the rupture section.

Tables:

Table 1. Chemical composition of tube

	C	Si	Mn	P	S	Cr	Ni	Nb	Fe
ASTM A213 Grade-TP347H	0.10 0.04	1.00 Max	2.00 Max	0.045 Max	0.030 Max	19.0 17.0	13.0 9.0	1.10 8$_x$C	Bal.
Actual chemical composition	0.06	0.45	1.84	0.012	0.006	17.1	10.4	0.7	Bal.

Table 2. The details of oil composition used for firing

Items	Standard	Unit	Mazut fuel
Carbon residue	D 189	Wt%	12.01
Ash content	D 482	Wt%	7.31
Sulfur content	D 129	Wt%	3.62
Water & sedi	D 96	Vol%	0.80
Na	D 6595	ppm	170.00
V	D 6595	ppm	56.00
Ca	D 6595	ppm	31.40
Ni	D 6595	ppm	22.80
Fe	D 6595	ppm	12.30
Mg	D 6595	ppm	5.70
Al	D 5695	ppm	2.20
Other elements	D 5695	ppm	2.70

Fig. 1. (a) Ruptured region of as-received superheater tube, and (b) the presence of white deposits on external surface.

12

Fig. 2. Thickness measurements for two sections of tube, (a) transverse cross-section far from failed region, and (b) failed region.

Fig. 3. Optical micrographs at mid-wall location of superheater tube far from failed region.

Fig. 4. SEM micrographs of transverse cross-section at mid-wall location.

Fig. 5. Corresponding EDS results of (a) arrow (A), and (b) arrow (B) in Fig. 4.

SEM MAG: 1.00 kx   WD: 23.20 mm   20 µm   VEGA\\ TESCAN
SEM HV: 15.00 kV   Det: BSE Detector
Date(m/d/y): 02/20/14   Vac: HiVac   RAZI
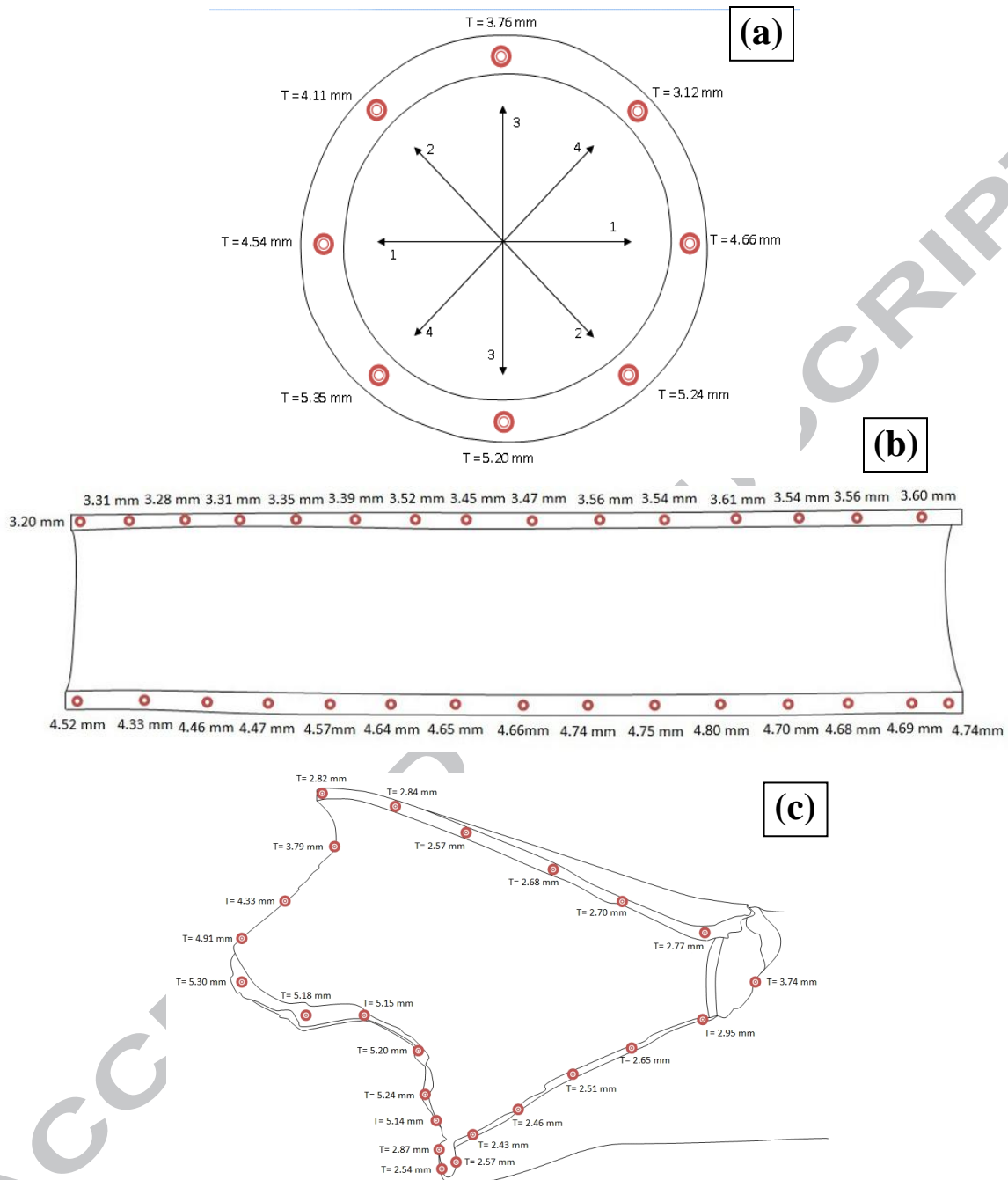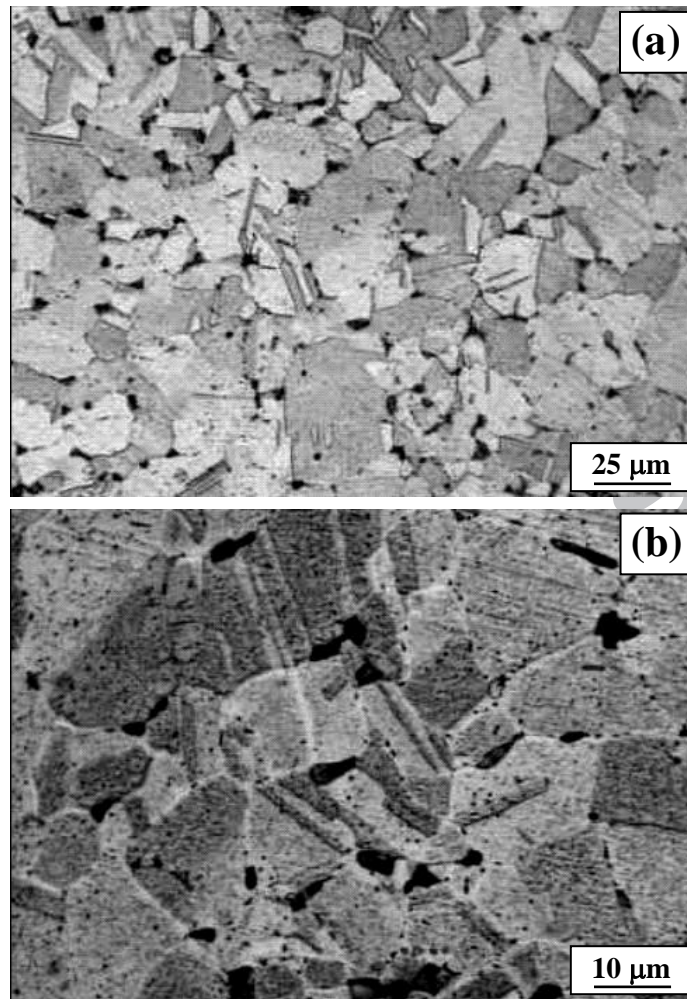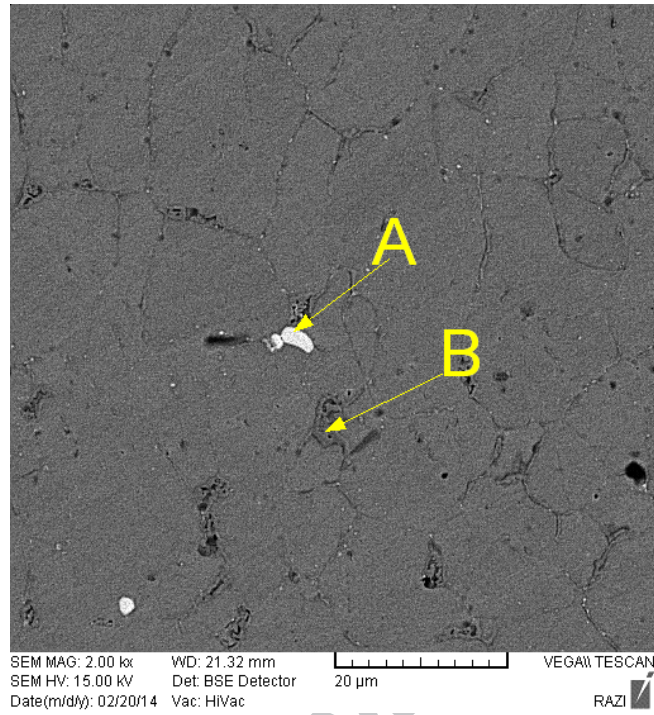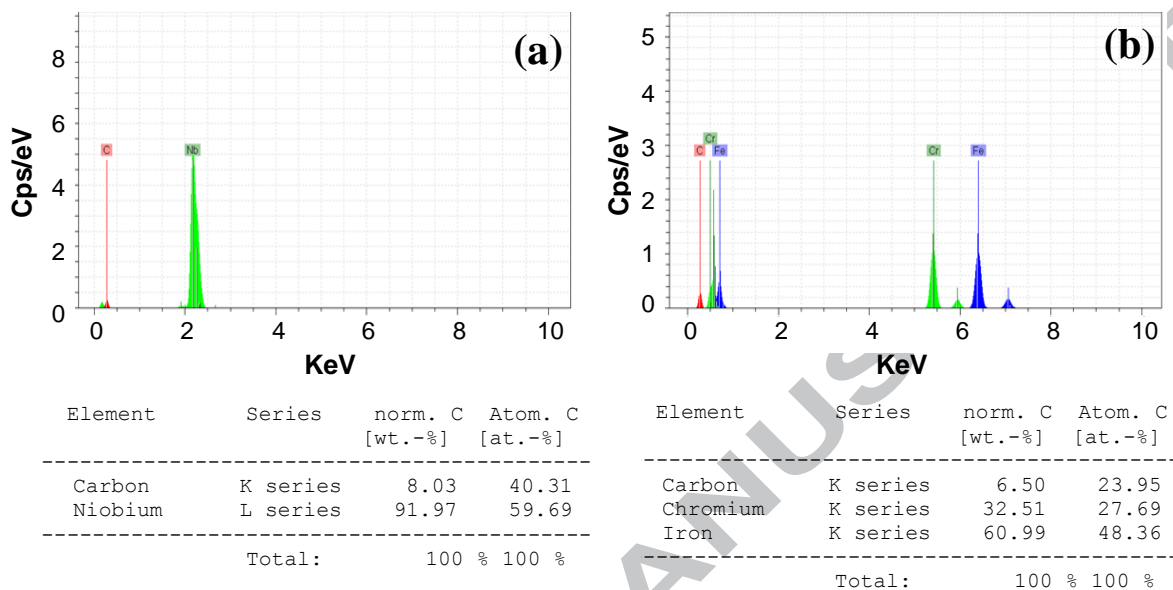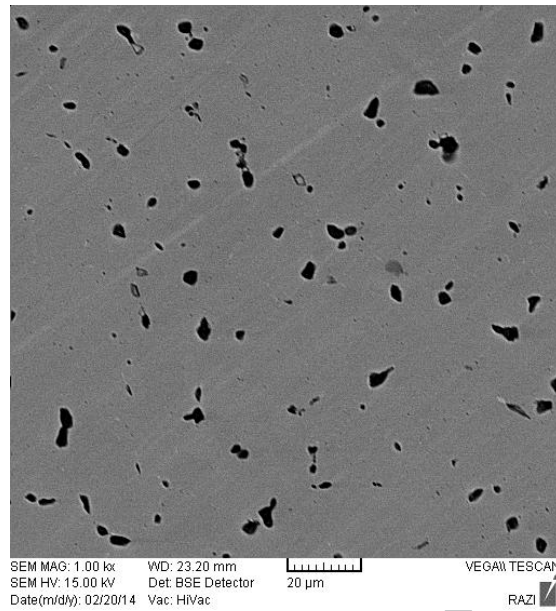
Fig. 6. SEM micrograph of longitudinal section.
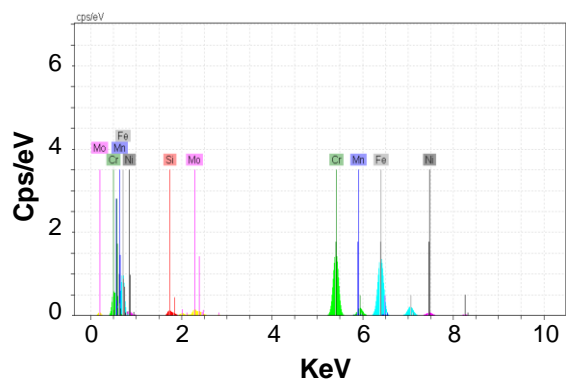
```
Element       Series    norm. C   Atom. C
                        [wt.-%]   [at.-%]
-------------------------------------------------
Silicon       K series    1.04      2.04
Chromium      K series   33.30     35.08
Manganese     K series    1.52      1.52
Iron          K series   56.46     55.38
Nickel        K series    4.42      4.12
Molybdenum    L series    3.26      1.86
-------------------------------------------------
                Total:   100 %  100 %
```

Fig. 7. Corresponding EDS results of sigma-phase particles in Fig. 6.
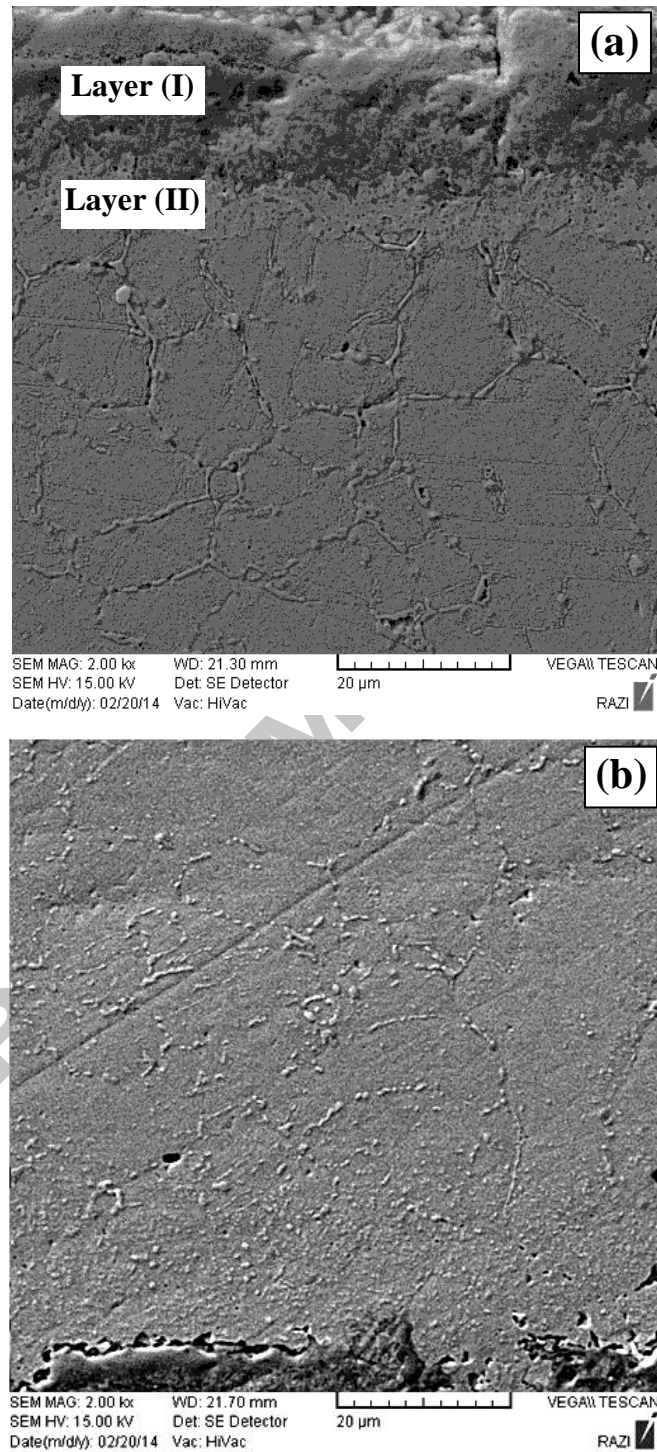
18

Fig. 8. SEM micrographs at the (a) outer diameter side, and (b) inner diameter side of tube.

```
Element      Series    norm. C   Atom. C
                       [wt.-%]   [at.-%]
-----------------------------------------
Oxygen       K series    28.64     58.03
Vanadium     K series     1.59      1.01
Chromium     K series    29.93     18.66
Iron         K series    27.83     16.15
Nickel       K series     9.58      5.29
Niobium      L series     2.44      0.85
-----------------------------------------
             Total:       100%    100 %
```

```
Element      Series    norm. C   Atom. C
                       [wt.-%]   [at.-%]
-----------------------------------------
Oxygen       K series    19.27     46.65
Silicon      K series     0.74      1.02
Chromium     K series    32.83     24.46
Iron         K series    19.27     13.37
Nickel       K series    12.70      8.38
Molybdenum   L series    15.18      6.13
-----------------------------------------
             Total:       100%    100 %
```

Fig. 9. Corresponding EDS results of (a) layer (I), and layer (II) in Fig. 8 (a).

20
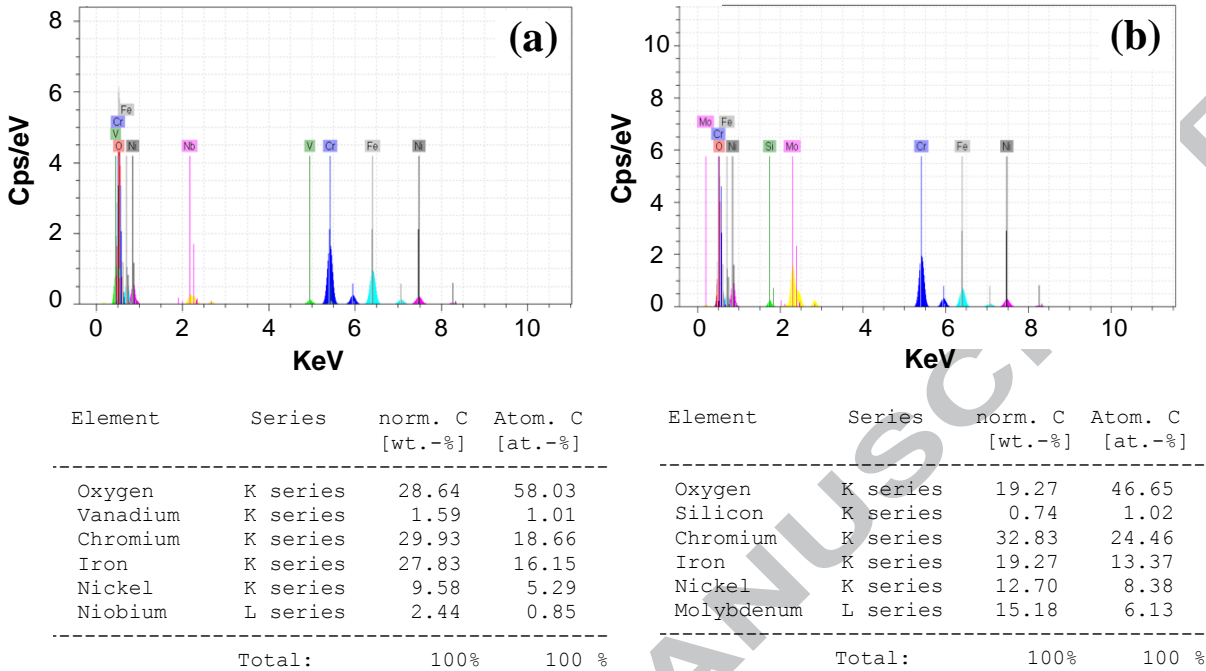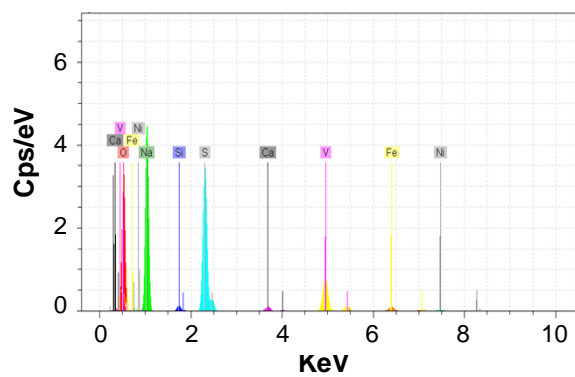
```
Element     Series     norm. C   Atom. C
                       [wt.-%]   [at.-%]
-----------------------------------------
Oxygen      K series    48.24     63.87
Sodium      K series    20.99     19.34
Silicon     K series     0.52      0.39
Sulfur      K series    15.89     10.50
Calcium     K series     0.62      0.33
Vanadium    K series    10.24      4.26
Iron        K series     2.51      0.95
Nickel      K series     0.99      0.36
-----------------------------------------
            Total:     100 % 100 %
```

Fig. 10. EDS analysis of loose scales on the external surface of tube.
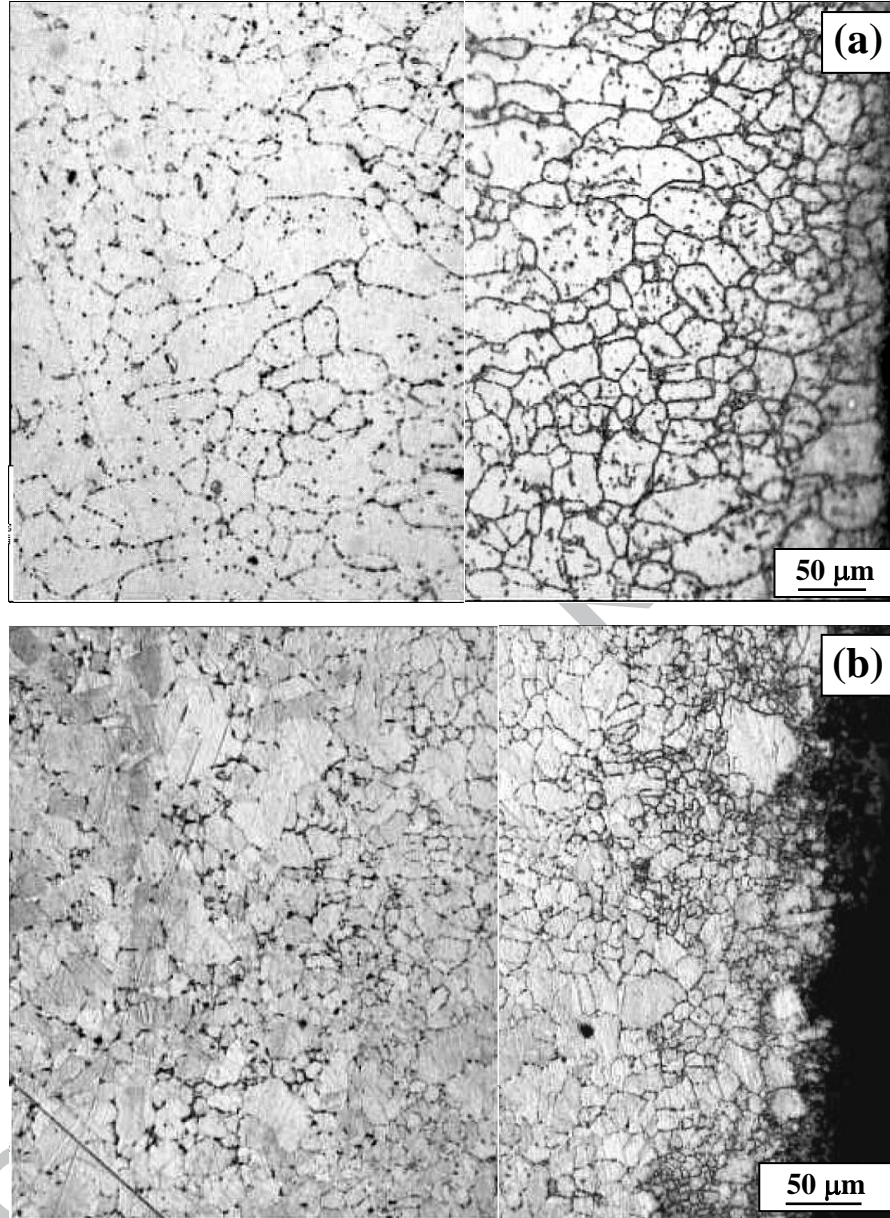
21

Fig. 11. Optical micrographs of (a) outer diameter, and (b) inner diameter of tube in order to illustrate incremental coagulation of carbides with approaching to the tube's surfaces.
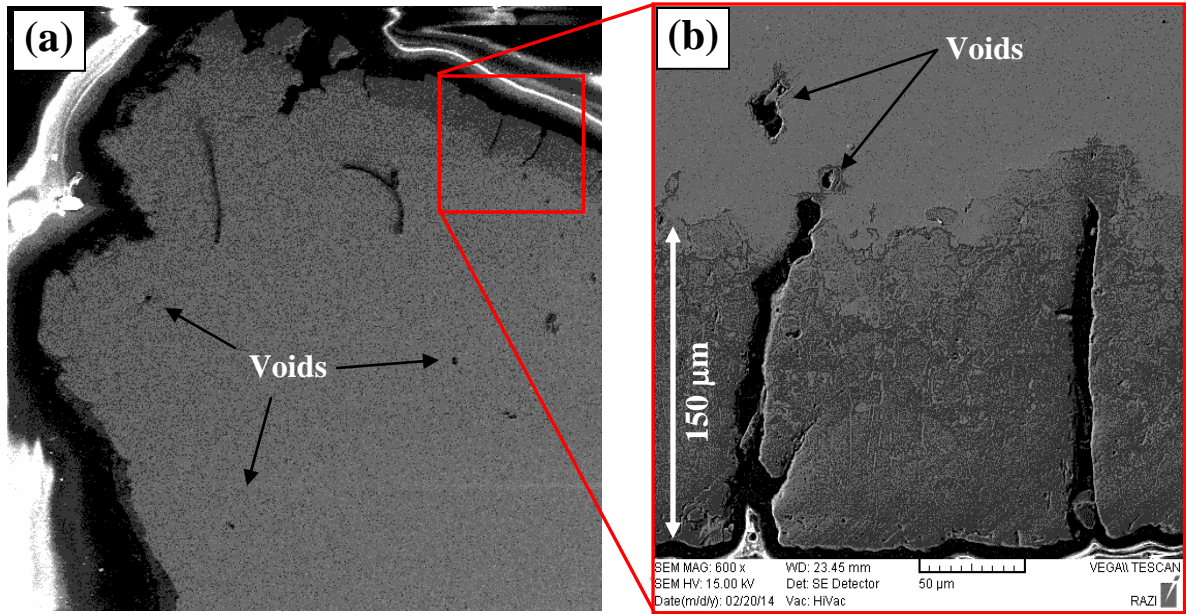
Fig. 12. SEM micrographs of failed region.
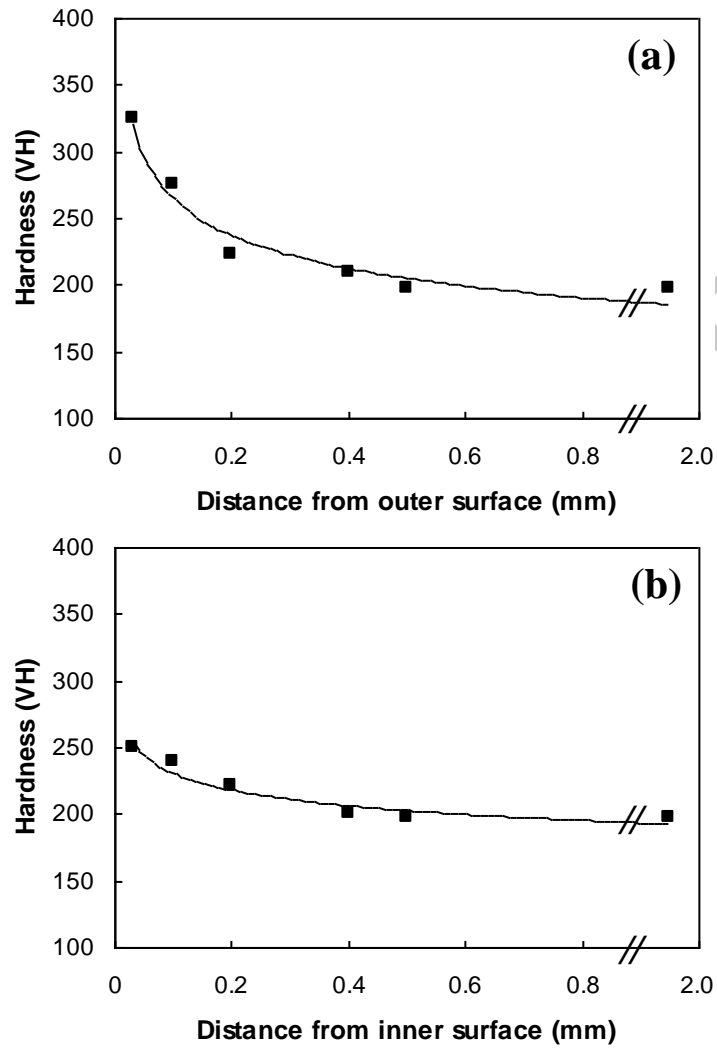
Fig. 13. Variation of microhardness against distance from (a) outer surface, and (b) inner surface.
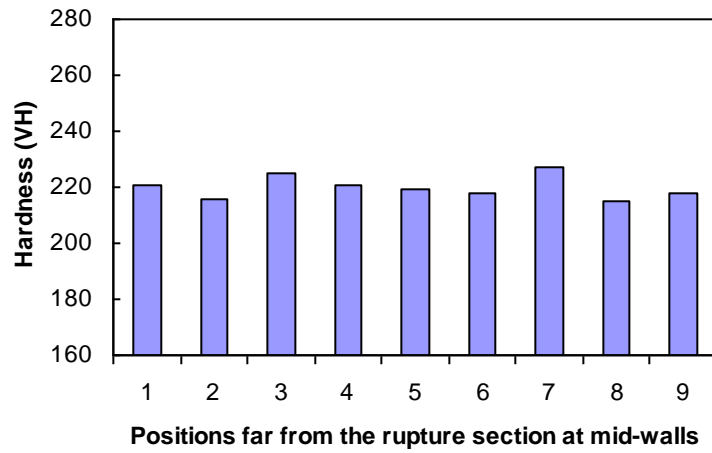
Fig. 14. The hardness measurements at some mid-walls away from the rupture section.

Highlights

Non- uniformity at the tube wall thickness far from the failed region was observed

Suggested main root cause of failure was fireside corrosion

Long-term overheating had worsened the tube condition during the service.

The formation of sigma-phase particles was revealed after 20 years service